Received: 15 August 2019 | Revised: 3 January 2020 | Accepted: 4 January 2020

DOI: 10.1002/mrm.28182

NOTE

Magnetic Resonance in Medicine

Intravoxel B_0 inhomogeneity corrected reconstruction using a low-rank encoding operator

Fan Lam[1,2,3] | **Bradley P. Sutton**[1,2,3]

[1]Department of Bioengineering, University of Illinois at Urbana-Champaign, Champaign, IL, USA

[2]Beckman Institute for Advanced Science and Technology, University of Illinois at Urbana-Champaign, Champaign, IL, USA

[3]Department of Electrical and Computer Engineering, University of Illinois at Urbana-Champaign, Champaign, IL, USA

Correspondence
Fan Lam, Beckman Institute for Advanced Science and Technology, University of Illinois at Urbana-Champaign, 405 N. Mathews Ave, Urbana, IL 61801 USA.
Email: fanlam1@illinois.edu

Funding information
National Institutes of Health, Grant/Award Number: R01DE027989

Purpose: To present a general and efficient method for macroscopic intravoxel B_0 inhomogeneity corrected reconstruction from multi-TE acquisitions.

Theory and Methods: A signal encoding model for multi-TE gradient echo (GRE) acquisitions that incorporates 3D intravoxel B_0 field variations is derived, and a low-rank approximation to the encoding operator is introduced under piecewise linear B_0 assumption. The low-rank approximation enables very efficient computation and memory usage, and allows the proposed signal model to be integrated into general inverse problem formulations that are compatible with multi-coil and undersampling acquisitions as well as different regularization functions.

Results: Experimental multi-echo GRE data were acquired to evaluate the proposed method. Effective reduction of macroscopic intravoxel B_0 inhomogeneity induced artifacts was demonstrated. Improved R_2^* estimation from the corrected reconstruction over standard Fourier reconstruction has also been obtained.

Conclusions: The proposed method can effectively correct the effects of intravoxel B_0 inhomogeneity, and can be useful for various imaging applications involving GRE-based acquisitions, including fMRI, quantitative R_2^* and susceptibility mapping, and MR spectroscopic imaging.

KEYWORDS

inhomogeneity correction, image reconstruction, intravoxel B_0 inhomogeneity, low-rank models, multi-echo acquisitions

1 | INTRODUCTION

MR acquisitions using multiple gradient echoes (GREs) have a wide range of applications, including functional MRI, quantitative R_2^* and susceptibility mapping, myelin water imaging, fat/water imaging, and even general MR spectroscopic imaging.[1-7] As these acquisitions sample signal evolutions along the free induction decay, they inherently encode signals related to both tissue-dependent properties and macroscopic B_0 field inhomogeneity. While the first is generally the signal of interest, the latter often introduces significant artifacts in the reconstructed images as well as errors in the subsequent quantitative analysis due to intravoxel dephasing and additional echo-time (TE) dependent signal distortions.[6-9] A straightforward approach to address this issue is to decrease the voxel size by extending k-space coverages,[10,11] thus reducing intravoxel B_0 variations, but at the expense of longer acquisitions and increased susceptibility to system instability and motion.

A number of signal processing–based methods have also been proposed to mitigate the effects of macroscopic intravoxel B_0 field inhomogeneity for GRE acquisitions. One main approach is to derive voxel-wise TE-dependent modulation functions originating from B_0 inhomogeneity and apply post-reconstruction correction by removing these modulations from the data or incorporating them into the parameter fitting model.[6-9,12-16] However, the voxel-wise modulation function is reconstruction-method dependent and can be rather difficult to derive for advanced reconstruction techniques which yield more complicated point-spread functions. An alternative approach is to perform B_0 corrected reconstruction by incorporating field inhomogeneity modeling into the imaging equation and solving the corresponding inverse problem. Such an approach is more general but can be very computationally expensive if intravoxel B_0 variations are considered.[17,18] Therefore, most methods have been limited to 2D acquisitions and assumed constant B_0 distributions within each voxel.[19-24] Through-plane B_0 variations have been considered with slice profile modeling for non-Cartesian readouts,[25] but limited to single-TE, 2D scans while ignoring in-plane intravoxel inhomogeneity.

In this work, we developed a new method for efficient 3D intravoxel B_0 inhomogeneity corrected reconstruction that can be flexibly adapted to different acquisition strategies and allows the use of different regularization functions. Specifically, we derived a signal encoding model for multi-TE GRE acquisitions that incorporates 3D intravoxel B_0 variations, and introduced a low-rank approximation to the encoding operator under a piecewise linear inhomogeneity assumption, enabling very efficient computation of the forward model. The new encoding model can be incorporated into general inverse problem formulations for B_0 corrected reconstruction, compatible with both multi-coil and undersampled acquisitions. Experimental multi-echo GRE data have been acquired to evaluate the proposed method. Effective reduction of intravoxel B_0 inhomogeneity induced image artifacts was demonstrated along with improved R_2^* estimation from the corrected reconstruction over standard Fourier reconstruction. We expect the proposed method to be useful for various imaging applications involving T_2^* contrast, including fMRI, quantitative R_2^* and susceptibility mapping, fat/water imaging and general MR spectroscopic imaging.

2 | THEORY

2.1 | Signal model

A general signal encoding model for multi-echo GRE acquisitions can be written as follows (ignoring the phase evolution during each short readout period):

$$d_c(\mathbf{k}, TE) = \int_{-\infty}^{\infty} s_c(\mathbf{r})\rho(\mathbf{r}, TE)e^{i2\pi\Delta f(\mathbf{r})TE}e^{-i2\pi\mathbf{k}^T\mathbf{r}}d\mathbf{r} + n_c(\mathbf{k}, TE) \tag{1}$$

where $\rho(\mathbf{r}, TE)$ is the function of interest with TE being the echo time, $\Delta f(\mathbf{r})$ the macroscopic B_0 field inhomogeneity, $s_c(\mathbf{r})$ the coil sensitivity profile, $n_c(\mathbf{k}, TE)$ the measurement noise, $\mathbf{r} = [x, y, z]^T$ and $\mathbf{k} = [k_x, k_y, k_z]^T$ are vectors denoting the spatial and k-space coordinates, respectively. Discretizing ρ using voxel basis function $\phi_n(\mathbf{r}) = \phi(\mathbf{r} - n\Delta\mathbf{r})$ (with $\Delta\mathbf{r}$ being the voxel size) while assuming piecewise constant sensitivity maps leads to

$$\begin{aligned} d_c(\mathbf{k}_m, TE) &= \int_{-\infty}^{\infty} \sum_{n=1}^{N} s_{c,n}c_n(TE)\phi(\mathbf{r} - n\Delta\mathbf{r})e^{i2\pi\Delta f(\mathbf{r})TE}e^{-i2\pi\mathbf{k}_m^T\mathbf{r}}d\mathbf{r} + n_c(\mathbf{k}_m, TE) \\ &= \sum_{n=1}^{N} s_{c,n}c_n(TE)\int_{-\infty}^{\infty} \phi(\mathbf{r} - n\Delta\mathbf{r})e^{i2\pi\Delta f_n(\mathbf{r})TE}e^{-i2\pi\mathbf{k}_m^T\mathbf{r}}d\mathbf{r} + n_c(\mathbf{k}_m, TE), \end{aligned} \tag{2}$$

where m and n are the k-space sample and voxel indices, respectively, $c_n(TE)$ denotes the signal intensity for the nth voxel at TE and $\Delta f_n(\mathbf{r})$ captures the field inhomogeneity variations within the nth voxel. While a common choice for $\phi(\mathbf{r})$ is the rectangular basis, denoted as $\phi(\mathbf{r}) = \text{rect}(x/\Delta x)\text{rect}(y/\Delta y)\text{rect}(z/\Delta z)$, evaluation of the integration in Equation 2 with an arbitrary $\Delta f_n(\mathbf{r})$ can be rather difficult. One straightforward solution is to let $\Delta f_n(\mathbf{r})$ be constant within individual voxels, which however is only accurate for very high-resolution acquisitions and can lead to significant image artifacts for lower-resolution data or at regions with strong field inhomogeneity. Another strategy is to assume a certain parametric form for $\Delta f_n(\mathbf{r})$. Specifically, if a locally linear assumption is used, that is,

$$\Delta f_n(\mathbf{r}) = f_n + \mathbf{g}_n^T\mathbf{r}, \quad \mathbf{g}_n = [g_{nx}, g_{ny}, g_{nz}]^T, \tag{3}$$

with $\mathbf{g}_n$ being the intravoxel field gradient at the nth voxel and the rectangular (box-car) voxel basis is chosen, Equation 2 can be rewritten as

$$d_c(\mathbf{k}_m, TE) = \sum_{n=1}^{N} s_{c,n}e^{i2\pi f_n TE}c_n(TE)e^{-i2\pi\mathbf{k}_m^T\mathbf{r}_n}\mathbf{W}_{mn}(TE) + n_c(\mathbf{k}_m, TE), \tag{4}$$

where

$$\mathbf{W}_{mn}(TE) = \mathrm{sinc}[(k_{mx} - g_{nx}TE)\Delta x]\mathrm{sinc}[(k_{my} - g_{ny}TE)\Delta y]\mathrm{sinc}[(k_{mz} - g_{nz}TE)\Delta z]. \quad (5)$$

The sinc functions arise from Fourier transform of the voxel basis functions modulated by intravoxel linear phases due to B_0 inhomogeneity. This encoding operator can also be extended to consider B_0 effects during each readout (ignored in this work for multi-echo GRE acquisitions), by replacing TE with $TE + t_m$ in the above equations where t_m denotes the sampling time for the mth k-space point. It can be seen that directly evaluating the forward model in Equation 4 for high-resolution 3D reconstruction is memory prohibitive and computationally expensive because the coupling between the elements in $\mathbf{W}$ and $e^{-i2\pi\mathbf{k}_m^T\mathbf{r}_n}$ prevents direct application of FFT. However, we will show in the subsequent sections that efficient computation can be derived by exploiting the fact that $\mathbf{W}$ can be well approximated by a low-rank matrix.

2.2 | Low-rank approximation of the encoding operator

The encoding matrix $\mathbf{W}$ being approximately low rank can be motivated by an examination of its elements. Consider a 1D case where $\mathbf{W}_{mn}(TE) = \mathrm{sinc}[(k_{mx} - g_{nx}TE)\Delta x]$, it can be seen that different columns in $\mathbf{W}$ are essentially a set of shifted sinc functions evaluated at $k'_{mx} - \delta k_{nx}$ ($k'_{mx} = k_{mx}\Delta x$ and $\delta k_{nx} = g_{nx}\Delta x TE$). Furthermore, for a practical B_0 map, the intravoxel B_0 gradients have a distribution that can be captured by a few representative values. As a result, all the shifted sinc functions have strong linear correlation, leading to the approximately low-rankness of $\mathbf{W}$. This is illustrated in Supporting Information Figure S1. Figure 1 shows the intravoxel field gradients along all three spatial directions obtained from an experimentally acquired B_0 field map, calculated using first-order finite differences of neighboring voxels (Figure 1A), and demonstrates the low-rank property of the encoding matrix $\mathbf{W}$ constructed from these field gradient maps. Specifically, we synthesized a $\mathbf{W}$ using g_{nx}, g_{ny} and g_{nz} corresponding to a single slice (Constructing the encoding matrix $\mathbf{W}$ for the entire 3D volume is memory prohibitive.), from which the singular values were computed and shown in Figure 1B. As can be seen, the singular values of $\mathbf{W}$ decay very rapidly, indicating that it can be accurately approximated by a low-rank matrix. Accordingly, for each TE, we can approximate $\mathbf{W}(TE)$ using the following low-rank factorization[26-29]

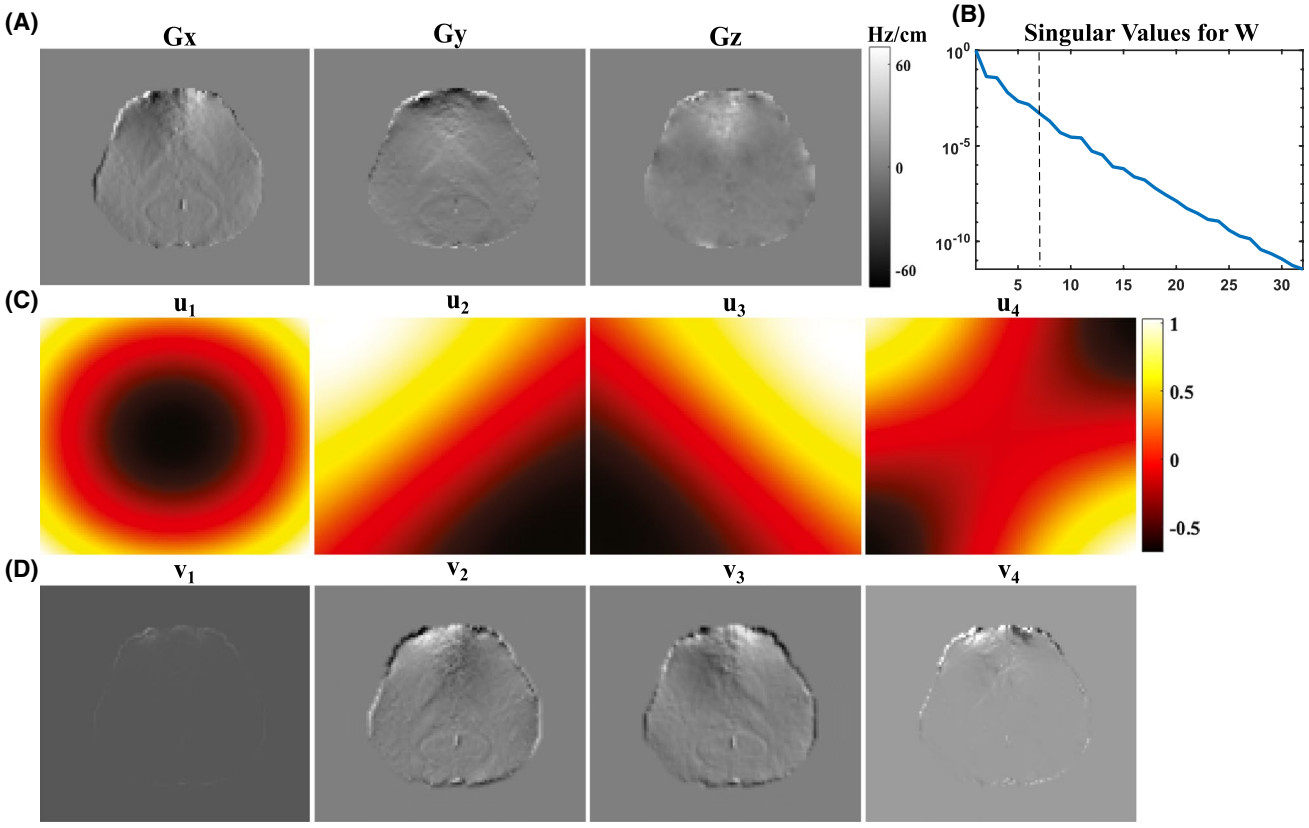

FIGURE 1 Low-rank decomposition of the $\mathbf{W}$ matrix in the proposed encoding model: A, maps of intravoxel field gradients calculated from an experimentally acquired B_0 map (shown for a single slice and the horizontal direction is the x direction); B, the first 32 singular values for a $\mathbf{W}$ constructed using the field gradients in (A); C,D, illustrations of $\mathbf{u}_l$ (k-space weighting) and $\mathbf{v}_l$ (spatial modulation) corresponding to the first four singular values of $\mathbf{W}$. The rapid singular value decay in (B) validates the low-rank approximation of $\mathbf{W}$, with the dash line indicating where the approximation error falls below 0.1%. Note that the y-axis in (B) is in log scale

$$\mathbf{W}(TE) \approx \mathbf{UV} = \sum_{l=1}^{L} \mathbf{u}_l(TE)\mathbf{v}_l^T(TE), \quad L \ll M, N \tag{6}$$

where $\mathbf{U} \in \mathcal{R}^{M \times L}$ and $\mathbf{V} \in \mathcal{R}^{L \times N}$ are two rank-L matrices, $\{\mathbf{u}_l\}_{l=1}^{L} \in \mathcal{R}^M$ and $\{\mathbf{v}_l\}_{l=1}^{L} \in \mathcal{R}^N$ are the columns in $\mathbf{U}$ and rows in $\mathbf{V}$, respectively (This low-rank factorization can be connected to singular value decomposition (SVD) of $\mathbf{W}$, where the singular values are incorporated into $\mathbf{U}$ (as scaling factors for individual columns) or $\mathbf{V}$ (as scaling factors for individual rows).), M is the number of k-space samples and N is number of voxels in an image. As can be seen, the operation specified by $\mathbf{W}$ is decomposed into L components, each of which contains a voxel-wise multiplication between the image and $\mathbf{v}_l$, and a k-space point-wise multiplication with $\mathbf{u}_l$. Figure 1C,D display the first four $\mathbf{u}_l$ and $\mathbf{v}_l$ components obtained from an SVD of the $\mathbf{W}$ described above, to help visualize their spatial and k-space modulation effects (each of these vectors were reshaped into images and the scaling effects of singular values on $\mathbf{u}_l$ were removed for display purpose). With this approximation, we can avoid explicit storage and computation of $\mathbf{W}$ and enabling the use of FFT in the forward model evaluation. More specifically, Equation 4 can be rewritten in the following matrix-vector multiplication form

$$\begin{aligned} \mathbf{d}_{c,TE} &= \sum_{l=1}^{L} \mathbf{u}_l(TE) \odot \{\mathbf{F}_\Omega(\mathbf{v}_l(TE) \odot \mathbf{S}_c \boldsymbol{\rho}_{TE})\} + \mathbf{n}_{c,TE} \\ &= \mathbf{E}_{c,TE}\boldsymbol{\rho}_{TE} + \mathbf{n}_{c,TE} \end{aligned} \tag{7}$$

where $\mathbf{d}_{c,TE}$ is a vector containing the measured data from the cth coil for image $\boldsymbol{\rho}_{TE}$ (a vector containing all the image coefficients), $\mathbf{S}_c$ captures the sensitivity map as well as the spatially dependent phase term $e^{i2\pi f_n TE}$ (as a diagonal matrix), $\mathbf{F}_\Omega$ is the Fourier encoding operator with sampling mask Ω, $\odot$ denotes a Hadamard product (point-wise multiplication) and $\mathbf{n}_{c,TE}$ is the noise vector. This reformulation allows a dramatic memory and computational complexity reduction for model-based intravoxel B_0 corrected reconstruction. Particularly, consider a reconstruction size of $128 \times 128 \times 32$, a complete storage of $\mathbf{W}$ requires 2 TB memory and the computational complexity for directly evaluating $\mathbf{W}$ is $\mathcal{O}(10^{11})$. Using the proposed approximation with a rank 8, the memory requirement is reduced to only 64 MB and the complexity with Equation 7 is reduced to $\mathcal{O}(10^8)$, enabling dramatic computation acceleration. Supporting Information Table S1 further highlights these improvements.

2.3 | Image reconstruction

With the signal equation in Equation 7, intravoxel B_0 inhomogeneity corrected reconstruction can be obtained by solving the following regularized least-squares formulation

$$\{\hat{\boldsymbol{\rho}}_{TE}\} = \underset{\{\boldsymbol{\rho}_{TE}\}}{\operatorname{argmin}} \sum_{TE} \sum_{c} \left\| \mathbf{d}_{c,TE} - \mathbf{E}_{c,TE}\boldsymbol{\rho}_{TE} \right\|_2^2 + \lambda R(\{\boldsymbol{\rho}_{TE}\}), \tag{8}$$

where the first term measures data consistency and the second term imposes certain regularization on the single/multi-TE images. Different choices are available for $R(\cdot)$. We chose $R(\{\boldsymbol{\rho}_{TE}\}) = \sum_{TE} \left\| \mathbf{T}\boldsymbol{\rho}_{TE} \right\|_2^2$, a spatial smoothness regularization to demonstrate the utility of the proposed corrected reconstruction method ($\mathbf{T}$ is a finite difference operator), while more sophisticated functions can be used. For example, since the proposed model and formulation supports joint multi-TE image reconstruction, a joint sparsity/edge constraint can be readily incorporated.[30-33] For the quadratic regularization, the linear conjugate gradient algorithm can be applied to solve the problem in Equation 8 efficiently. We note that a similar low-rank approximation of the B_0 inhomogeneity operator has been previously described in Ref. [25] for single-TE, 2D fMRI reconstruction from long readouts, which considered through-slice B_0 variations. This work takes the complete 3D intravoxel B_0 variations into account and focuses on addressing their effects in multi-echo acquisitions.

3 | METHODS

3.1 | Estimation of $\{\mathbf{u}_l\}$ and $\{\mathbf{v}_l\}$

As the size of $\mathbf{W}$ can be prohibitively huge (of size M-by-N with M being the number of k-space samples and N being the number of voxels in the reconstruction), especially for 3D imaging, directly calculating $\{\mathbf{u}_l\}_{l=1}^{L}$ and $\{\mathbf{v}_l\}_{l=1}^{L}$ by performing SVD of $\mathbf{W}$ is impractical. However, given the explicit low-rank factorization, we can devise efficient ways to estimate $\{\mathbf{u}_l\}$ and $\{\mathbf{v}_l\}$ without accessing the full $\mathbf{W}$. This has been demonstrated in the partial separability (PS)-based dynamic imaging methods.[26-29] Specifically, modeling $\mathbf{W}$ as $\mathbf{W} = \mathbf{UV}$ implies that the columns of $\mathbf{W}$ reside in a low-dimensional subspace specified by $\mathbf{U}$. Thus, the columns in $\mathbf{U}$ can be treated as a basis of this subspace and $\mathbf{V}$ as the corresponding coefficients. Therefore, we can first synthesize a subset of the columns in $\mathbf{W}$ by randomly sampling the field gradient maps (denoted as ($g_x(\mathbf{r})$, $g_y(\mathbf{r})$ and $g_z(\mathbf{r})$) within the signal regions, and obtain an estimate of $\mathbf{U}$ by performing an SVD to these randomly sampled columns (i.e., 5000) and selecting the L dominant left singular vectors and singular values. The rank L was chosen by inspecting the singular value decay such that the truncation error was less than 0.5%. With $\mathbf{U}$ estimated, we can then synthesize a subset of the rows in $\mathbf{W}$ by randomly sampling k-space locations and estimate $\mathbf{V}$ by performing a least-squares fitting using the corresponding rows in $\mathbf{U}$. The minimum number of rows needed is L but we randomly selected 400 coordinates in the 3D k-space to ensure a sufficiently good condition number for the estimation of $\mathbf{V}$. We found that for a typical 3D brain B_0 map, the estimation error for $\mathbf{U}$ and $\mathbf{V}$ using such a scheme is less than

0.1% compared to directly applying SVD to a complete **W** matrix (details shown in Supporting Information Figure S2). We also would like to note that our low-rank encoding operator and the above estimation scheme are conceptually similar to the histogram principle component analysis based approximation of complex exponential functions described in Ref. [21], which only considered constant B_0 in each voxel for 2D non-Cartesian acquisitions.

3.2 | Multi-echo implementation

The proposed model and reconstruction can readily be extended to acquisitions with many echoes. Specifically, the B_0 maps can be estimated directly from the multi-TE data, for example, by performing a parametric fitting to an initial/low-resolution reconstruction. TE-dependent $\mathbf{u}_l(TE)$ and $\mathbf{v}_l(TE)$ can be estimated for individual $\mathbf{W}(TE)$'s using the estimation strategy described above. Two new sets of matrices, $\{\mathbf{U}_l\} \in \mathcal{R}^{M\times P}$ and $\{\mathbf{V}_l\} \in \mathcal{R}^{N\times P}$ (with P being the number of TEs), can then be constructed, each of which contains the k-space and spatial modulation vectors for all the TEs and the lth component. Accordingly, Equation 7 can be extended as

$$\mathbf{D}_c = \sum_{l=1}^{L} \mathbf{U}_l \odot \{\mathbf{F}_\Omega(\mathbf{V}_l \odot \mathbf{S}_c\mathbf{X})\} + \mathbf{N}_c, \tag{9}$$

where the N-by-P matrix $\mathbf{X}$ contains the images for all TEs (ie, $\mathbf{X} = [\boldsymbol{\rho}_1, \boldsymbol{\rho}_2, \ldots, \boldsymbol{\rho}_P]$) and the M-by-P matrices $\mathbf{D}$ and $\mathbf{N}$ contain the measured data and noise for all TEs, respectively. As a result, efficient implementations for joint multi-TE B_0 corrected reconstruction can be performed, which can be easily scaled up to higher-dimensional imaging problems such as MRSI acquisitions with many echoes. For the cases with multiple or many TEs, a sparsity and low-rank constraint can also be imposed on the unknown TE-dependent image sequence $\mathbf{X}$.

3.3 | Data acquisition

Simulations and in vivo experiments were performed to evaluate the proposed method. For simulation, a single-TE image and a B_0 map were first obtained from an experimentally acquired 3D multi-TE GRE scan (with a matrix size of $256 \times 256 \times 40$ and a voxel size of $0.9 \times 0.9 \times 1.5\,\text{mm}^3$). The magnitude image $|\mathbf{I}(\mathbf{r})|$ was taken and the B_0 map was subject to a piecewise linear fit. A new complex-valued image was then synthesized by combining the magnitude image and phase introduced by the fitted B_0 map $\Delta f(\mathbf{r})$ as follows: $\mathbf{I}(\mathbf{r}) = |\mathbf{I}(\mathbf{r})|e^{i2\pi\Delta f(\mathbf{r})TE}$, with TE being the echo time of the original acquisition. A high-resolution single-slice 2D image (256×256) and a low-resolution version with k-space truncated to 128×128 were first used to evaluate the proposed B_0 corrected reconstruction with a full $\mathbf{W}$ as well as the low-rank approximation. A set of low-resolution k-space data ($128 \times 128 \times 20$ matrix size) was subsequently simulated for the full 3D reconstruction tests. For in vivo experiments, high-resolution (HR) multi-echo 3D GRE data ($0.9 \times 0.9 \times 1.5\,\text{mm}^3$ voxel size) and accompanying low-resolution (LR) scans ($2 \times 2 \times 3\,\text{mm}^3$ voxel size) were acquired on a 3 T Siemens Prisma scanner (Siemens Healthineers, Erlangen, Germany) equipped with a 20-channel head coil. The other imaging parameters are: TR = 68 ms, TE = [4.1, 7.6, 11.1, 14.6, 18.1, 21.6, 25.1, 28.6, 33.0, 45.0] ms (10 echoes), FOV = $220 \times 220 \times 72$, flip angle = 15° and bandwidth/pixel = 520 Hz. All experiments were performed with approval from local Institutional Review Board and participants' consent.

4 | RESULTS

Figure 2 shows the reconstruction results from the simulated single-slice data. The regularization parameter λ for the proposed reconstruction was chosen using the discrepancy

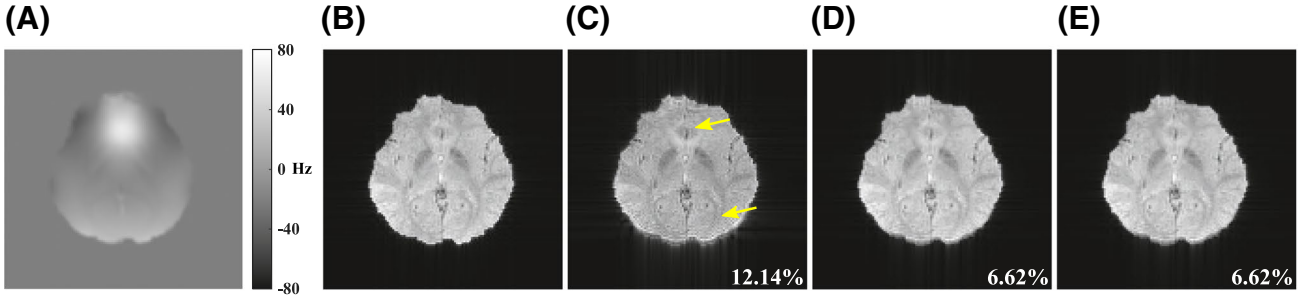

FIGURE 2 Comparison of reconstructions from a 2D single-slice simulation data with B_0 map illustrated in (A); B, reconstruction from the high-resolution data (with a k-space truncation after removing the phase); C, direct Fourier reconstruction from the low-resolution data; D, B_0 corrected reconstruction using the full $\mathbf{W}$ matrix; and E, the proposed reconstruction using a rank-8 approximation of $\mathbf{W}$. Relative l_2 errors using the image in (B) as a reference are also shown (in the bottom right corners) for a quantitative evaluation. Effective artifact reduction (as highlighted by the yellow arrows in B) and quantitative improvement were achieved by the proposed method

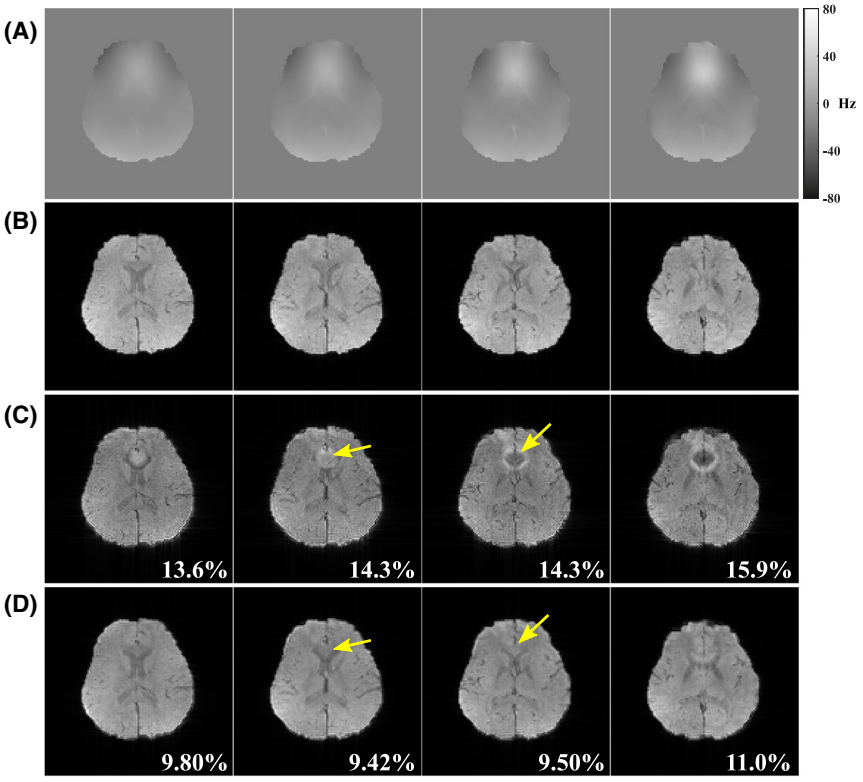

FIGURE 3 Simulation results (3D): A, the B_0 maps used in the simulation (from experimental data); B, images reconstructed from a truncated k-space of the high-resolution magnitude image (without intravoxel B_0 effects and treated as the "gold standard"); C, a direct Fourier reconstruction from the 128 × 128 × 20 low-resolution k-space data (no intravoxel B_0 correction); and D, the proposed reconstruction from the same low-resolution data. Different columns show images at different slices (images towards the right are closer to the sinus area). Effective artifact reduction was achieved by the proposed method (as indicated by the yellow arrows). Quantitative improvement is demonstrated using the relative ℓ_2 errors shown in the bottom right corner of the images

principle. The B_0 map used in this simulation is shown in Figure 2A and the reconstructed magnitude images are compared in Figure 2B-E. Specifically, a "reference" (Figure 2B) was generated by truncating the k-space of the high-resolution magnitude image (from 256 × 256 to a 128 × 128 k-space coverage). As the phase has been removed before k-space truncation, there is no intravoxel B_0 effects. A direct Fourier reconstruction of the low-resolution k-space data from the complex-valued image was shown in Figure 2C, and the results produced by the proposed method in Figure 2D (reconstruction using the full **W**) and Figure 2E (reconstruction using a rank-8 approximation of **W**). Relative l_2 errors with respect to the reference image were also calculated for a quantitative evaluation. As can be seen, the proposed method effectively reduced the image artifacts in the direct Fourier reconstruction of low-resolution data caused by intravoxel B_0 inhomogeneity, and produced a more accurate reconstruction. The low-rank approximated encoding operator yielded almost the same results as using the full **W**. Reconstructions from this simulation data using approximated **W** at different ranks are further compared in the Supporting Information Figure S3. The results remain similar for a range of Ls.

A set of 3D reconstruction results, with and without the proposed B_0 corrected reconstruction using the low-rank encoding operator, are shown in Figure 3. Different axial slices across the 3D volume are shown. Compared to the Fourier reconstruction of the low-resolution k-space data, the proposed method significantly reduced the image artifacts and signal loss due to the 3D intravoxel B_0 variations. Similar to the 2D case, the proposed method produced quantitatively more accurate results compared to the Fourier reconstruction (as demonstrated by the l_2 errors calculated using the k-space truncated high-resolution magnitude image as the reference).

Figure 4 compares the reconstructions from an in vivo multi-echo GRE data. The B_0 map used for correction is shown in Figure 4A. Similar to the comparison in simulation, a reference was obtained by first removing the phase in the HR image (from the HR data) and truncating the k-space (in Figure 4B). A direct Fourier reconstruction and the proposed reconstruction with intravoxel B_0 correction ($L = 10$) from the LR data are also shown (Figure 4C,D). As can be seen, the HR data has minimal intravoxel dephasing due to the smaller voxel size, while the LR Fourier reconstruction has apparent artifacts in regions with strong B_0 inhomogeneity variations. The proposed method effectively reduced these artifacts, producing similar images as the reconstruction from HR data. R_2^* maps were also estimated from the three different reconstructions and compared in Figure 5, along with signal decay curves chosen from two representative voxels. Significant artifact reduction as well as better matching signal decays to the HR data can also be observed for the proposed method, further demonstrating its utility in improving subsequent quantitative analysis for multi-echo GRE acquisitions. An additional set of reconstruction from another in vivo data (from a different volunteer) is shown in Supporting Information Figure S4 to further demonstrate the effectiveness of the proposed method. The residual artifacts observed in the

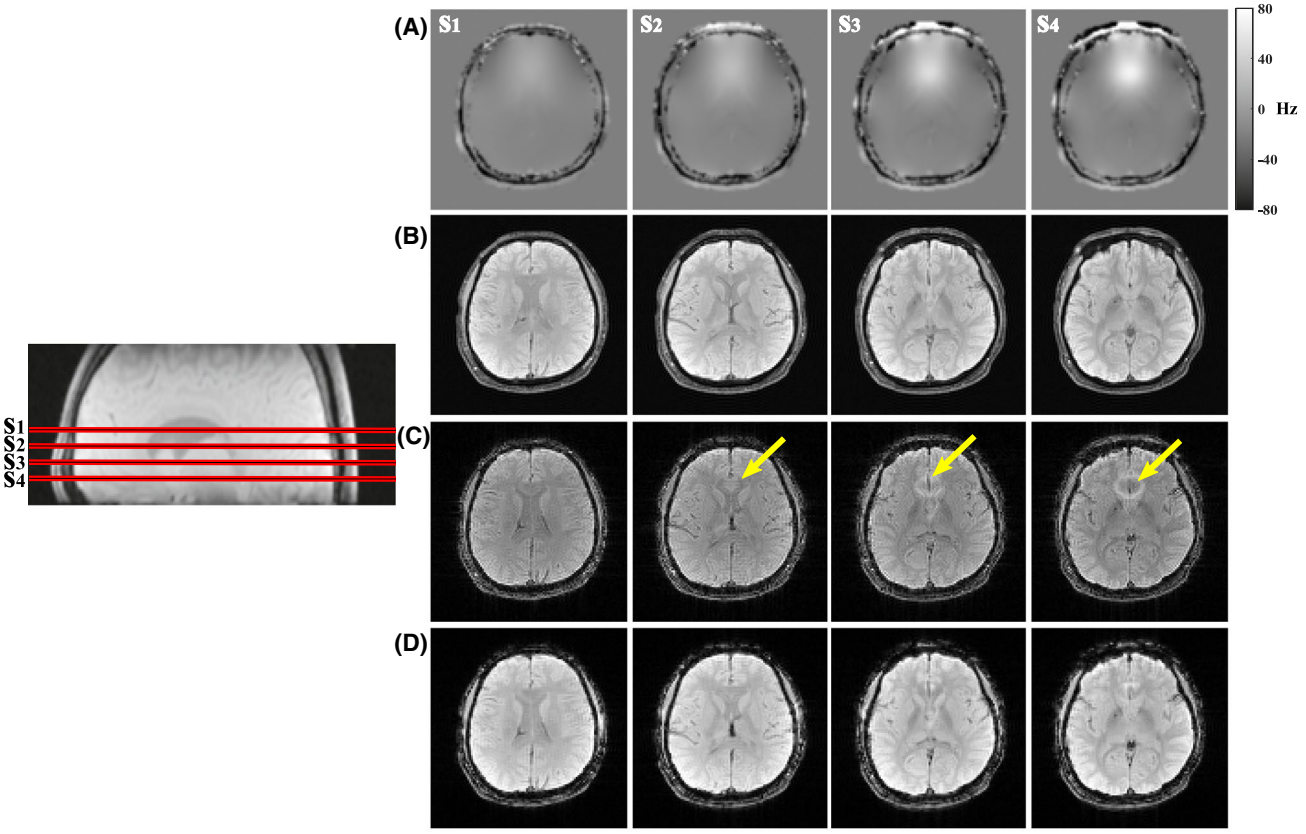

FIGURE 4 Results from the in vivo multi-echo GRE data: A, B_0 maps for different slices across the 3D volume; B, reconstructed images for the corresponding slices at a specific TE (25.1 ms) from the HR data (k-space truncation after removing phases at the original resolution); C, direct Fourier reconstruction from the LR data; D, the proposed reconstruction from the LR data. The HR reconstruction has minimal intravoxel dephasing induced artifacts due to a small voxel size. The LR Fourier reconstruction has apparent B_0 induced artifacts which were reduced by the proposed reconstruction. The slice locations are indicated by the red lines in a sagittal view of the 3D volume shown on the left

corrected reconstructions are likely caused by errors in the field maps, estimated field gradients, and potentially inaccuracy of the piece-wise linear model in voxels with significant B_0 variations.

5 | DISCUSSION AND CONCLUSION

We have developed a new reconstruction method for macroscopic intravoxel B_0 inhomogeneity correction. The proposed method incorporates the effects of intravoxel field variations into the data acquisition model and introduces a low-rank approximation to the resulting encoding operator, enabling efficient memory usage, computation, and integration into any regularized reconstruction formulation. Effective during-reconstruction B_0 inhomogeneity correction for multi-echo GRE data have been demonstrated with reduced intravoxel dephasing induced artifacts and improved quantitative R_2^* estimation. We expect the proposed method to be useful for a range of applications involving T_2^* contrast and multi-echo GRE acquisitions.

The current model only includes TE dependence in the encoding operator **W** and ignores the time evolution for the k-space data acquired during each readout, which should be considered for EPI or spiral type of acquisitions with longer readouts. However, the proposed method can be readily extended to these scenarios by incorporating sampling time dependence into different rows of **W** and estimating the low-rank factorization accordingly. Another approach is to introduce the time dimension (or the FID dimension) and reformulate the reconstruction problem in a higher dimensional (k,t)-space. Similar strategies have been recently proposed for multi-shot EPI-based imaging,[34] where the multi-shot EPI reconstruction was formulated as a multi-TE imaging problem with sparse sampling. In this case, the time dependence in the k-space sampling can be mapped to the TE dimension in our multi-TE formulation, which will allow for potential incorporation of different constraints on the unknown multi-TE images for improved reconstruction. The proposed low-rank encoding operator can also be applied to joint R_2^* mapping and image reconstruction problems as described in Ref. [23,35] and allow more efficient computation.

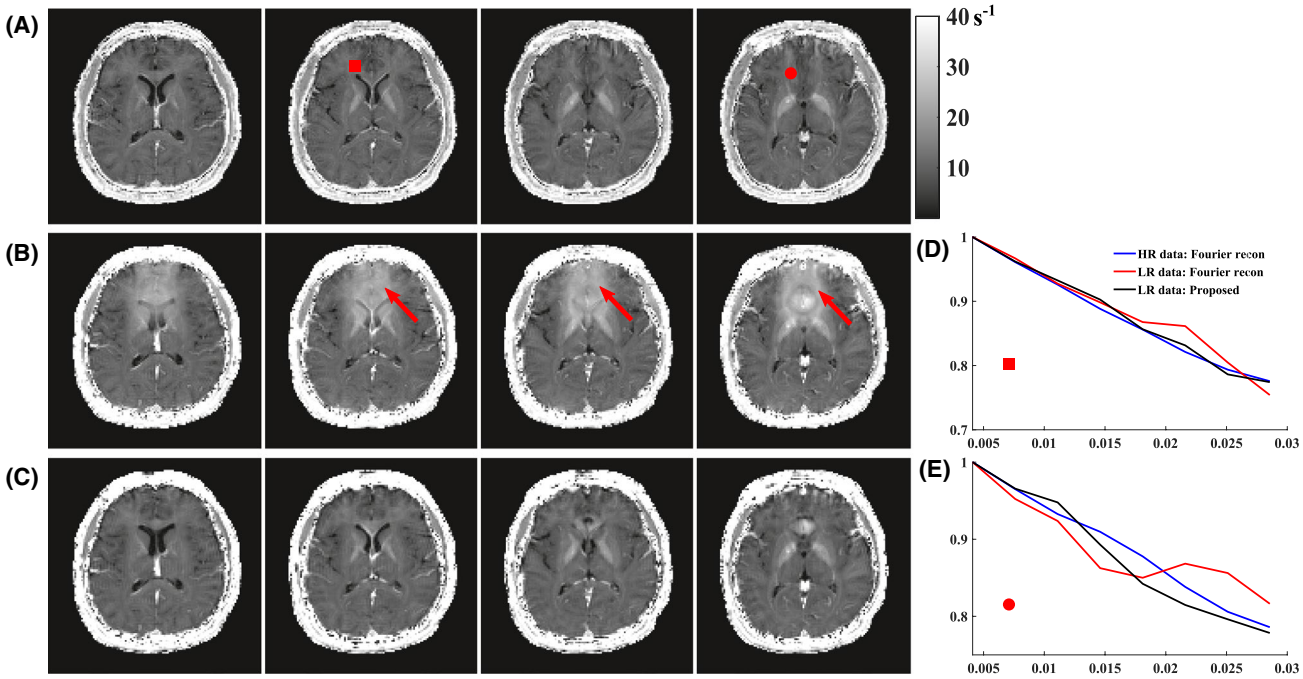

FIGURE 5 R_2^* maps obtained from the reconstructions in Figure 4. The maps obtained from the HR reconstruction, LR Fourier reconstruction, and the proposed reconstruction are shown in (A) to (C), respectively, for four slices. The signal decays for two representative voxels are shown in (D) and (E) to further illustrate the correction effects. The locations of the voxels are marked by symbols with different shapes in (A). The proposed method yielded more consistent signal variations along TE to the HR data than the LR reconstruction

While the well-defined sinc function kernels in the encoding matrix **W** are the result of rectangular voxel basis and piece-wise linear B_0 inhomogeneity models, we expect that **W** should still be approximately low rank with choices of other voxel bases, eg, Gaussian or triangle functions. In this case, different columns in **W** will just be products of many shifted Gaussian or squared-sinc functions with strong correlation. The use of higher-order intravoxel B_0 functions can lead to much more complicated expressions of **W**, some even without an analytical form, which needs to be investigated with more rigors in future research.

It should be pointed out that in this work we used a B_0 map initially estimated from the low-resolution data to calculate the field gradients, while a more accurate high-resolution B_0 map will lead to more accurate field gradient estimates thus improving the correction or even allowing the incorporation of more complicated intravoxel field variations. We would also like to note that the proposed method shares conceptual similarities with the time/frequency-segmentation methods described in Ref. [36] and a more general version described in Ref. [21] where essentially a low-rank based approximation was applied to the complex exponential function $e^{i2\pi\Delta f_n t}$ with Δf_n and t denoting the field inhomogeneity value at the nth voxel and readout time vector, respectively, without considering intravoxel B_0 variations. Combinations of these methods to address the problem of reconstruction from long readouts, especially for non-Cartesian trajectories, are interesting extensions to investigate in follow-up research.

ACKNOWLEDGMENTS

The research reported in this publication was supported in part by the National Institute of Dental and Craniofacial Research of the National Institutes of Health under Award Number R01DE027989. The content is solely the responsibility of the authors and does not necessarily represent the official views of the National Institutes of Health. This work was conducted in part at the Biomedical Imaging Center of the Beckman Institute for Advanced Science and Technology at the University of Illinois at Urbana-Champaign (UIUC-BI-BIC).

ORCID

Fan Lam http://orcid.org/0000-0002-4124-0663

REFERENCES

1. Kundu P, Voon V, Balchandani P, Lombardo MV, Poser BA, Bandettini PA. Multi-echo fMRI: a review of applications in fMRI denoising and analysis of BOLD signals. *NeuroImage*. 2017;154:59–80.
2. Ordidge RJ, Gorell JM, Deniau JC, Knight RA, Helpern JA. Assessment of relative brain iron concentrations using T_2-weighted and T_2^*-weighted MRI at 3 Tesla. *Magn Reson Med*. 1994;32:335–341.
3. Wang Y, Liu T. Quantitative susceptibility mapping (QSM): decoding MRI data for a tissue magnetic biomarker. *Magn Reson Med*. 2015;73:82–101.
4. Alonso-Ortiz E, Levesque IR, Pike GB. MRI-based myelin water imaging: a technical review. *Magn Reson Med*. 2015;73:70–81.

5. Du Y, Chu R, Hwang D, et al. Fast multislice mapping of the myelin water fraction using multicompartment analysis of T_2^* decay at 3T: a preliminary postmortem study. *Magn Reson Med*. 2007;58:865–870.
6. Hernando D, Vigen K, Shimakawa A, Reeder S. R_2^* mapping in the presence of macroscopic B_0 field variations. *Magn Reson Med*. 2012;68:830–840.
7. Posse S, Tedeschi G, Risinger R, Ogg R, Le Bihan D. High speed ^{1}H spectroscopic imaging in human brain by echo planar spatial-spectral encoding. *Magn Reson Med*. 1995;33:34–40.
8. Yablonskiy DA. Quantitation of intrinsic magnetic susceptibility-related effects in a tissue matrix. Phantom study. *Magn Reson Med*. 1998;39:417–428.
9. Fernandez-Seara MA, Wehrli FW. Postprocessing technique to correct for background gradients in image-based R_2^* measurements. *Magn Reson Med*. 2000;44:358–366.
10. Glover GH. 3D z-shim method for reduction of susceptibility effects in BOLD fMRI. *Magn Reson Med*. 1999;42:290–299.
11. Bellgowan PS, Bandettini PA, van Gelderen P, Martin A, Bodurka J. Improved BOLD detection in the medial temporal region using parallel imaging and voxel volume reduction. *NeuroImage*. 2006;29:1244–1251.
12. An H, Lin W. Cerebral oxygen extraction fraction and cerebral venous blood volume measurements using MRI: effects of magnetic field variation. *Magn Reson Med*. 2002;47:958–966.
13. Dahnke H, Schaeffter T. Limits of detection of SPIO at 3.0 T using T_2^* relaxometry. *Magn Reson Med*. 2005;53:1202–1206.
14. Yang X, Sammet S, Schmalbrock P, Knopp MV. Postprocessing correction for distortions in T_2^* decay caused by quadratic cross-slice B_0 inhomogeneity. *Magn Reson Med*. 2010;63:1258–1268.
15. Baudrexel S, Volz S, Preibisch C, et al. Rapid single-scan T_2^*-mapping using exponential excitation pulses and image-based correction for linear background gradients. *Magn Reson Med*. 2009;62:263–268.
16. Yablonskiy DA, Sukstanskii AL, Luo J, Wang X. Voxel spread function method for correction of magnetic field inhomogeneity effects in quantitative gradient-echo-based MRI. *Magn Reson Med*. 2013;70:1283–1292.
17. Sutton B, Noll D, Fessler J. Compensating for within-voxel susceptibility gradients in BOLD fMRI. In: Proceedings of Annual Meeting of ISMRM, Kyoto, Japan; 2004:349.
18. Zhuo Y, Sutton BP. Iterative image reconstruction model including susceptibility gradients combined with Z-shimming gradients in fMRI. In: Proceedings of Annual International Conference of the IEEE EMBS; 2009:5721–5724.
19. Sutton BP, Noll DC, Fessler JA. Fast, iterative image reconstruction for MRI in the presence of field inhomogeneities. *IEEE Trans Med Imaging*. 2003;22:178–188.
20. Noll DC, Fessler JA, Sutton BP. Conjugate phase MRI reconstruction with spatially variant sample density correction. *IEEE Trans Med Imaging*. 2005;24:325–336.
21. Fessler JA, Olafsson VT, Shi HR, Noll DC. Toeplitz-based iterative image reconstruction for MRI with correction for magnetic field inhomogeneity. *IEEE Trans Signal Process*. 2005;53:3393–3402.
22. Knopp T, Eggers H, Dahnke H, Prestin J, Senegas J. Iterative off-resonance and signal decay estimation and correction for multi-echo MRI. *IEEE Trans Med Imaging*. 2009;28:394–404.
23. Ngo GC, Sutton BP. R_2^* mapping for robust brain function detection in the presence of magnetic field inhomogeneity. In: Proceedings of 36th Annual International Conference of the IEEE EMBS; 2014:1537–1540.
24. Peng X, Nguyen H, Haldar JP, Hernando D, Wang XP, Liang ZP. Correction of field inhomogeneity effects on limited k-space MRSI data using anatomical constraints. In: Proceedings of IEEE Engineering in Medicine and Biology Society, Buenos Aires; 2010:883–886.
25. Fessler JA, Noll DC. Model-based MR image reconstruction with compensation for through-plane field inhomogeneity. In: Proceedings of IEEE International Symposium on Biomedical Imaging, Washington DC; 2007:920–923.
26. Liang ZP. Spatiotemporal imaging with partially separable functions. In: Proceedings of IEEE International Symposium on Biomedical Imaging, Washington DC; 2007:988–991.
27. Haldar JP, Hernando D. Rank-constrained solutions to linear matrix equations using power factorization. *IEEE Signal Process Lett*. 2009;16:584–587.
28. Zhao B, Haldar JP, Christodoulou AG, Liang ZP. Image reconstruction from highly undersampled (k, t)-space data with joint partial separability and sparsity constraints. *IEEE Trans Med Imaging*. 2012;31:1809–1820.
29. Christodoulou AG, Zhang H, Zhao B, Hitchens TK, Ho C, Liang Z. High-resolution cardiovascular MRI by integrating parallel imaging with low-rank and sparse modeling. *IEEE Trans Biomed Eng*. 2013;60:3083–3092.
30. Majumdar A, Ward RK. Accelerating multi-echo T_2 weighted MR imaging: analysis prior group-sparse optimization. *J Magn Reson*. 2011;210:90–97.
31. Haldar JP, Wedeen VJ, Nezamzadeh M, et al. Improved diffusion imaging through SNR-enhancing joint reconstruction. *Magn Reson Med*. 2013;69:277–289.
32. Zhao B, Lu W, Hitchens TK, Lam F, Ho C, Liang ZP. Accelerated MR parameter mapping with low-rank and sparsity constraints. *Magn Reson Med*. 2015;74:489–498.
33. Lai Z, Zhang X, Guo D, et al. Joint sparse reconstruction of multi-contrast MRI images with graph based redundant wavelet transform. *BMC Med Imaging*. 2018;18:7–22.
34. Wang F, Dong Z, Reese TG, et al. Echo planar time-resolved imaging (EPTI). *Magn Reson Med*. 2019;81:3599–3615.
35. Olafsson VT, Noll DC, Fessler JA. Fast joint reconstruction of dynamic R_2^* and field maps in functional MRI. *IEEE Trans Med Imaging*. 2008;27:1177–1188.
36. Noll DC, Meyer CH, Pauly JM, Nishimura DG, Macovski A. A homogeneity correction method for magnetic resonance imaging with time-varying gradients. *IEEE Trans Med Imaging*. 1991;10:629–637.

SUPPORTING INFORMATION

Additional Supporting Information may be found online in the Supporting Information section.

FIGURE S1 Illustration of the approximately low-rankness of $\mathbf{W}$ using a 1D case with elements $\mathbf{W}_{mn} = \text{sinc}\left[(k_m - g_{nx}TE)\Delta x\right]$: (A) A histogram of the B_0 field gradients from an experimentally acquired B_0 map. The x-axis denotes $\delta k_{nx} = g_{nx}TE\Delta x$; (B) Plots of different columns in $\mathbf{W}$. These curves have a strong linear dependence such that $\mathbf{W}$ can be well approximated by a low-rank matrix

FIGURE S2 Comparison of the low-rank decomposition $\mathbf{U}$ and $\mathbf{V}$ estimated using a direct SVD of the encoding matrix $\mathbf{W}$ and the proposed random sampling plus least-squares fitting scheme. The intravoxel B_0 field gradients for a

single 2D slice were used due to the memory requirement to store the complete **W** for SVD. As can be seen, the **U** and **V** estimated from these two different schemes show almost no difference. The relative ℓ_2 error is less than 0.1%

FIGURE S3 Comparison of B_0 corrected reconstructions from the 2D simulation data in Figure 2; Reconstruction using the full **W** matrix is shown in the first column and the reconstructions using low-rank approximations of **W** with different ranks (L) are shown in the subsequent columns. The results remain similar for a range of Ls as the rank truncation error is small (<1%), while too low of an L leads to noticeable artifacts, as expected for the case of $L = 2$ (truncation error >5%)

FIGURE S4 B_0 corrected reconstruction by the proposed method from data acquired from another volunteer. The acquisition parameters were the same as the data used to generate Figures 4 and 5. The arrangement is the same as in Figure 4

TABLE S1 Comparison of memory usage and computation complexity for directly evaluating **W** and the proposed low-rank approximation. M and N denote the numbers of k-space samples and reconstruction voxels, respectively. The numbers in the highlighted rows correspond to a reconstruction size of $128 \times 128 \times 32$ and $L = 8$. As L is orders of magnitude smaller than M or N, significant reduction in memory usage and computation is achieved

How to cite this article: Lam F, Sutton BP. Intravoxel B_0 inhomogeneity corrected reconstruction using a low-rank encoding operator. *Magn Reson Med*. 2020;84:885–894. https://doi.org/10.1002/mrm.28182